Mesoporous Materials

DOI: 10.1002/ange.200802487

A General Route to Diverse Mesoporous Metal Oxide Submicrospheres with Highly Crystalline Frameworks**

Chia-Kuang Tsung, Jie Fan, Nanfeng Zheng, Qihui Shi, Arnold J. Forman, Jianfang Wang, and Galen D. Stucky**

Metal oxide particles ranging in size from nanometers to micrometers and possessing unique catalytic, electronic, and optical properties are of great interest for a variety of applications. In particular, their performance in catalysis and photocatalysis, which is primarily determined by their chemical compositions, crystallinity, and surface areas, has recently received much attention. A high-yield synthetic route that is capable of producing both single- and multicomponent metal oxide spheres with high surface areas and crystallinity will undoubtedly benefit the design of high-performance materials in the catalyst industry.[1,2] The aerosol-assisted self-assembly process (AASA),[3,4] an integration of aerosol-spray and evaporation-induced assembly, is a very promising strategy. The aerosol-spray approach is the only existing process that allows for continuous, easy, and large-scale production of nanoparticulate materials. The evaporation-induced assembly is one of a few well-developed methods for synthesizing high-surface-area mesostructures with diverse metal oxide components.[5] Previous preparations using AASA have up to now been overwhelmingly dominated by silica-based materials.[6–12] Because the rapid-evaporation nature of the aerosol-spray process increases the difficulty in achieving the effective coupling between much more reactive non-siliceous sol–gel chemistry and surfactant-directed assembly, there have been only limited reports of mesoporous non-siliceous spheres produced by AASA.[13–16] Herein, we describe a simple, scalable synthetic strategy for the production of diverse single- and multicomponent, highly crystalline mesoporous metal oxide materials.

To develop a productive and general methodology for the preparation of submicrometer-sized mesostructured metal oxide spheres with highly crystalline frameworks, we have combined the acetic acid mediated sol–gel chemistry system, in which metal alkoxides are dissolved in mixture solutions of acetic acid, hydrochloric acid, and ethanol (AcHE),[17,18] together with the aerosol-assisted self-assembly approach. In the AcHE system, acetate ligands are bonded to the metal cores of metal alkoxides in a bidentate and bridging fashion to form stable, nanometer-sized metal oxo–acetate particles. These preformed precursor particles serve as inorganic building blocks, and are rapidly co-organized with organic amphiphilic block copolymers into ordered mesostructures during the evaporation process. The hydrolysis and condensation behaviors of these preformed precursor particles controlled by acetic acid are even able to enhance the mesostructure framework crystallinity at relatively low calcination temperatures while maintaining high surface areas. The AcHE system is also efficient at simultaneously controlling the sol-gel chemistry of multicomponent mixtures of metal alkoxide precursors to form stable precursor nanoparticles with similar sizes, which allows for the synthesis of homogeneous multicomponent mesoporous spheres.

Single-component mesoporous TiO_2, ZrO_2, and Al_2O_3 spheres with highly crystalline frameworks and multicomponent mesoporous 10% CuO–TiO_2, Al–Si–O, and $BaTiO_3$ spheres were chosen to demonstrate the generality of the approach. Figure 1a shows a typical scanning electron microscopy (SEM) image of the mesoporous metal oxide (TiO_2) spheres after calcination. The sphere size ranges from 50 nm to hundreds of nanometers, and they are free of surface cracks and intersphere adherence. These materials can be produced continuously at a rate of several grams per hour with our home-built spray system (see the Supporting Information, Figure S1). The uniform pore size distribution and close-packing configuration of the single-component TiO_2, ZrO_2, and Al_2O_3 spheres are clearly shown in the transmission electron microscopy (TEM) images (Figure 1b–d). Two diffraction peaks are resolved in their small-angle X-ray diffraction (SAXRD) patterns, indicating the long-range order of the porous structures (Figure 1e). Nitrogen adsorption measurements demonstrate that all the materials exhibit the type IV isotherm behavior with high Brunauer–Emmett–Teller (BET) surface areas ranging from 142 to 237 $m^2 g^{-1}$ (Table 1; see also the Supporting Information, Figure S2). The Barrett–Joyner–Halenda (BJH) pore sizes determined from the adsorption branches are around 3–5 nm, which is consistent with TEM characterizations.

In addition to their ordered mesostructures, another unprecedented feature of the mesoporous spheres prepared by AcHE is the facile creation of nanocrystal domain

---

[*] Dr. C.-K. Tsung, Dr. J. Fan, Dr. N. F. Zheng, Q. H. Shi, A. J. Forman, Prof. G. D. Stucky
Department of Chemistry and Biochemistry, University of California
Santa Barbara, CA 93106 (USA)
Fax: (+1) 805-893-4120
E-mail: stucky@chem.ucsb.edu
Prof. J. F. Wang
Department of Physics, The Chinese University of Hong Kong
Shatin, Hong Kong SAR (China)
Fax: (+852) 2603-5204
E-mail: jfwang@phy.cuhk.edu.hk

[**] This work was supported by the USA NSF (Grant No.: DMR 02-33728), the NASA URETI (Grant No.: NCC-1-02037), the HK RGC Research Grant Direct Allocation (Project Code: 2060332), and the NSFC/RGC Joint Research Scheme (Ref. No.: N_CUHK448/06, Project Code: 2900318).

Supporting information for this article is available on the WWW under http://dx.doi.org/10.1002/anie.200802487.

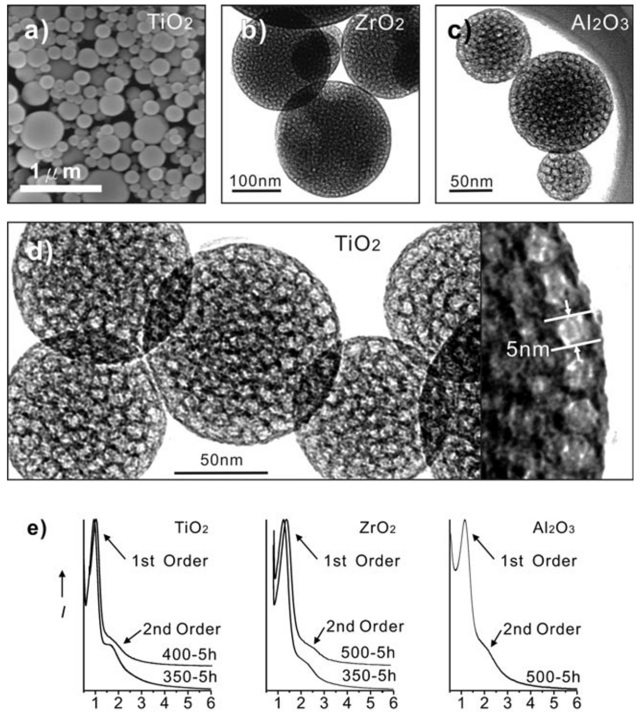

Figure 1. Mesoporous metal oxide spheres. a) SEM image of mesoporous TiO_2 spheres calcined at 350 °C for 5 h. b) TEM image of mesoporous ZrO_2 spheres calcined at 350 °C for 5 h. c) TEM image of mesoporous Al_2O_3 spheres calcined at 500 °C for 5 h. d) TEM image of mesoporous TiO_2 spheres calcined at 350 °C for 5 h. The inset shows that the measured pore sizes are in agreement with those determined from nitrogen adsorption measurements. e) SAXRD patterns of mesoporous TiO_2, ZrO_2, and Al_2O_3 spheres calcined under different conditions. The appearance of second-order diffraction peaks suggests the presence of highly ordered mesostructures.

Table 1: Crystalline and porous properties of mesoporous metal oxide spheres.

Product	Calcination T/t [°C/h]	Crystallinity	d[a] [nm]	Pore size[b] [nm]	Surface area[c] [m^2g^{-1}]	Pore volume[d] [cm^3g^{-1}/vol %]
Al_2O_3	500/5	amorphous	7.6	4.6	142	0.14/36
Al_2O_3	800/10	γ-alumina	N/A	4.1	112	0.08/24
ZrO_2	350/5	tetragonal	7.1	3.8	192	0.17/49
ZrO_2	500/5	tetragonal	6.3	3.1	146	0.11/38
TiO_2-I	350/5	anatase	9.3	4.8	237	0.28/53
TiO_2-II	350/5	anatase	9.4	4.6	218	0.27/52
TiO_2-III	350/5	anatase	9.4	4.5	229	0.28/53
TiO_2-400	400/5	anatase	8.4	3.8	154	0.23/48
Al–Si–O	800/20	amorphous	8.9	4.7	287	0.34
10%CuO–TiO_2	350/5	anatase	10.1	6.7	238	0.35
$BaTiO_3$	550/2	perovskite	N/A	15.8	29	0.16/48

[a] *d* values of the first-order diffraction peaks for the metal oxide spheres after calcination. [b] BJH pore sizes determined from the nitrogen adsorption branches. [c] BET surface areas determined from the nitrogen adsorption and desorption isotherm measurements. [d] Pore volumes (vol %) are calculated from the densities of the frameworks.

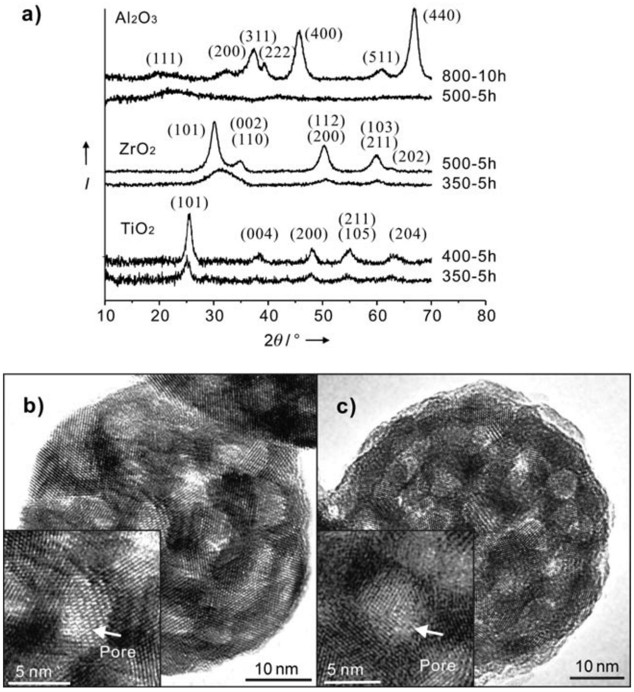

Figure 2. Highly crystalline frameworks. a) WAXRD patterns of single-component mesoporous metal oxide spheres calcined under different conditions. The diffraction peaks of TiO_2 are indexed to anatase, those of ZrO_2 are indexed to the tetragonal phase, and those of Al_2O_3 are indexed to the γ-alumina phase. b) HRTEM images of mesoporous ZrO_2 spheres calcined at 500 °C for 5 h. c) HRTEM images of TiO_2 spheres calcined at 400 °C for 5 h. The insets in (b) and (c) are zoomed-in images. The clear mesostructures and lattices in HRTEM images indicate the coexistence of mesostructure and high crystallinity.

frameworks at relatively low calcination temperatures. As illustrated in Figure 2a, the nanocrystals of anatase TiO_2 and tetragonal ZrO_2 are already formed in the frameworks when calcined at 350 °C, a rather low temperature, for 5 h. The crystallinity is further enhanced by increasing the calcination temperature to 400 and 500 °C for TiO_2 and ZrO_2, respectively. The nanocrystal sizes estimated from X-ray diffraction (XRD) peaks by the Scherrer formula are 8.0 and 4.9 nm, respectively. The high crystallinity of the mesoporous TiO_2 and ZrO_2 spheres is also confirmed by the clear lattices observed by high-resolution (HR) TEM imaging (Figure 2b,c). It is interesting to point out that the tetragonal zirconia phase exists only when the nanocrystal size is less than 30 nm at room temperature,[19] which is in agreement with our observation (4.9 nm). The framework of the mesoporous Al_2O_3 spheres remains amorphous after calcination at 500 °C for 5 h. The wide-angle (WA) XRD patterns clearly show that γ-Al_2O_3 nanocrystals of 5.3 nm in size are formed in the framework after calcination at 800 °C for 10 h. The absence of SAXRD peaks indicates the deterioration of the mesostructural ordering during the crystallization of the γ-Al_2O_3 framework. The maintenance of the high surface area (Table 1), however, confirms the coexistence of polycrystalline frameworks and porous structures. Compared to TiO_2

and ZrO_2, the higher crystallization temperature and easier deterioration of the Al_2O_3 mesostructure might be due to the complex sequence of the transformations during crystallization.[20]

The AcHE system has also been successfully applied to the synthesis of multicomponent mesoporous metal oxide spheres. Two crucial requirements for the preparation of multicomponent mesoporous spheres are to homogenously distribute each component in the precursor solution and to avoid macroscopic phase separation during solvent evaporation. Fortunately, the nature of our method can satisfy these requirements. The uniform distribution of the nanometer-sized precursor particles of different chemical compositions promises high homogeneity; the fast evaporation and assembly prevent local phase separation. Three different types of multicomponent mesoporous spheres, that is, 10% CuO–TiO_2, Al–Si–O, and $BaTiO_3$, are demonstrated. The energy dispersive X-ray (EDX) measurement confirms that the molar ratios of these calcined multicomponent mesoporous spheres are close to the initial compositions of the precursor solutions. Mesoporous 10% CuO–TiO_2 spheres are used to demonstrate the ability to homogeneously introduce extrinsic metal oxide components into crystalline metal oxide frameworks. Both SAXRD measurements (Figure 3b) and TEM images (see the Supporting Information, Figure S3d) reveal that the ordered mesostructure of CuO–TiO_2 spheres is still preserved even after the addition of as much as 10 mol% Cu^{2+}. Similar to the single-component mesoporous TiO_2 spheres, the highly crystalline anatase framework of 10% CuO–TiO_2 spheres is also confirmed by WAXRD. At 350°C, the formation of the anatase phase with no crystalline CuO peaks is seen (Figure 3a). According to previous studies, CuO nanocrystals can form at temperatures as low as 300°C.[21,22] We believe that the amorphous CuO component is homogeneously distributed in the TiO_2 framework.

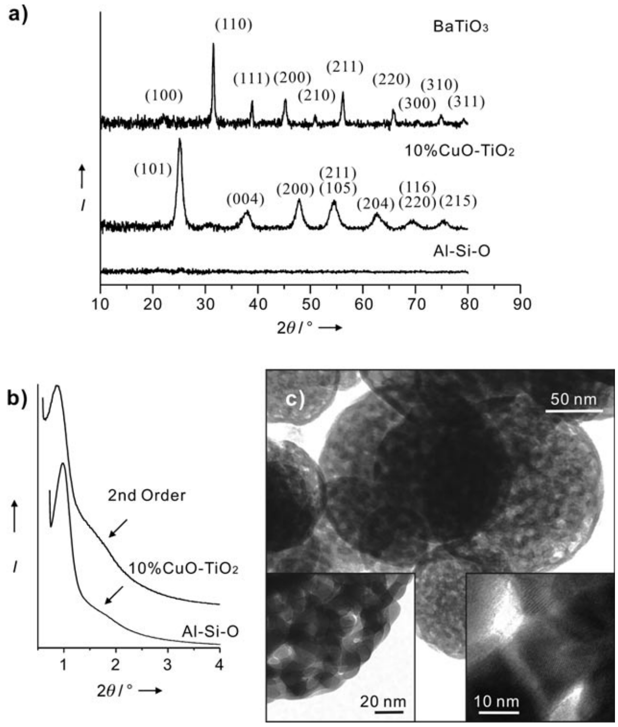

Figure 3. Multicomponent mesoporous metal oxide and bimetallic oxide spheres. a) WAXRD patterns. The diffraction peaks of 10% CuO–TiO_2 are indexed to anatase, and those of $BaTiO_3$ are indexed to perovskite. b) SAXRD patterns of mesoporous Al–Si–O and 10% CuO–TiO_2 spheres. c) TEM images of mesoporous $BaTiO_3$ spheres with a worm-like structured framework and high crystallinity. The insets are zoomed-in images.

Another step toward multicomponent spheres is to synthesize mixed metal oxide frameworks with local stoichiometric homogeneity. Owing to the dissimilar hydrolysis and condensation behaviors of silicon and aluminum alkoxides, the synthesis of mesoporous Al–Si–O spheres has not yet been reported. As expected, the introduction of the AcHE system can successfully circumvent this dissimilarity problem and lead to the formation of ordered mesoporous spheres (Figure 3b). These Al–Si–O mesoporous spheres have excellent thermal stability. The ordered mesostructure together with high surface areas is remained even after 20 h thermal treatment at 800°C of the Al–Si–O spheres with the Al/Si molar ratio of 1:1 (Table 1; see also the Supporting Information, Figure 3c). The absence of WAXRD peaks (Figure 3a) indicates the amorphous nature of the framework owing to the local stoichiometric homogeneity, which is consistent with previous studies.[23] These highly thermally stable, acidic metal oxide mesoporous spheres hold enormous potential for catalytic applications.

Porous bimetallic oxide $BaTiO_3$ spheres with perovskite nanocrystals in the framework have also been synthesized. The preparation of these bimetallic oxide spheres is synthetically complicated, because more accurate local stoichiometry and bonding are required. We therefore use bimetallic alkoxides $BaTi[OCH_2CH(CH_3)OCH_3]_6$ as the precursor to prepare perovskite $BaTiO_3$ spheres. In this case, neither HCl nor HNO_3 is suitable as a strong acid for the synthesis owing to the low solubility of $BaCl_2$ and $Ba(NO_3)_2$. The absence of strong acids makes the cooperative assembly of the block copolymer and inorganic species more difficult because of the lack of strong electrostatic interactions between inorganic and organic species. Alternatively, relatively higher quantities of block copolymers have been used to control the mesophase assembly. The TEM images (Figure 3c) confirm the worm-like structure, with a surface area of 29 $m^2 g^{-1}$ after calcination at 550°C for 2 h. The WAXRD pattern (Figure 3a) and HRTEM image (Figure 3c, inset) indicate that the worm-like framework is composed of circa 20 nm perovskite $BaTiO_3$ nanocrystals. No TiO_2 crystalline phase is observed. The larger framework domain in the worm-like structure, which is due to the use of a larger amount of block copolymers, provides the space for stabilizing the 20 nm-sized nanocrystals.

The low-temperature crystallization of the frameworks produced by our synthetic method deserves a more in-depth study. In our synthesis, a strong acid (HCl) is used, which functions as a catalyst for the esterification of acetic acid with the solvent, ethanol, to produce water. The water that is produced promotes the partial loss of the acetate ligands, which then induces the growth of metal oxo–acetate nanoparticles in the starting solution owing to the much lower stability of the metal–alkoxide bonds. The precursor nanoparticles generated then serve as building blocks and are organized with amphiphilic block copolymers into mesostructures. It is reasonable to believe that these larger nanometer-sized precursor particles in the as-made organic–inorganic hybrid mesostructures play an important role in the enhancement of the crystallization of calcined frameworks. On the basis of this, excess water was introduced directly to the precursor solutions to promote the growth of the precursor particles and therefore enhance the crystallinity. The crystallization and mesostructures of the calcined products were characterized, as demonstrated with TiO_2. Dynamic light scattering (DLS) was employed to follow the growth of the precursor particles in the solutions. The DLS size is different from and generally less well-defined than that obtained from small-angle X-ray scattering. However, DLS allows for good time-resolution without the use of synchrotron X-ray sources. The precursor solutions with H_2O (excess)/Ti ratios of 0, 10, and 20 were monitored by DLS after water introduction, and named TiO_2-I, TiO_2-II, and TiO_2-III, respectively. The DLS measurements indicate a uniform condensation and growth behavior in the precursor solutions (Figure 4a). Nanometer-sized precursor particles were detected rapidly after the introduction of controlled quantities of water. They are stable and their size increases as the relative amount of water is increased. The average stable sizes of the precursor particles are 3.5, 4.4, and 6.5 nm for TiO_2-I, TiO_2-II, and TiO_2-III, respectively. It is important to mention that the excess quantity of water influences the mesostructure assembly process. Such high quantities of water for evaporation-induced self-assembly are rarely reported. In our system, it is easy to remove excess water from the atomized precursor droplets by just increasing the temperature of the assembly chamber to 120 °C. The WAXRD patterns (Figure 4c) reveal the evolution of the crystallinity of the frameworks after the materials were calcined at 350 °C for 5 h. With increasing amounts of water in the precursor solution, the crystallization of the frameworks is enhanced. The peak intensities of TiO_2-III are as strong as those of TiO_2-400 (the sample prepared without introducing extra water and calcined at 400 °C for 5 h; Figure 2a). Highly ordered structures and high surface areas are confirmed by the second-order peaks in the SAXRD patterns (Figure 4b) and nitrogen adsorption measurements. The fixed peak positions and slight decrease in intensity indicate that the ordering of the mesoporous structure decreases slightly with increasing framework crystallinity. Detailed studies reveal that the introduction of excess water significantly increases the crystallinity of the frameworks of different samples, while the nanocrystal sizes remain fixed at around 6 nm for TiO_2-I, TiO_2-II, and TiO_2-III. In short, the addition of excess water to the synthesis allows for the coexistence of ordered mesostructures and highly crystalline frameworks without the use of high calcination temperatures typically required, which are well known to degrade mesostructured ordering.

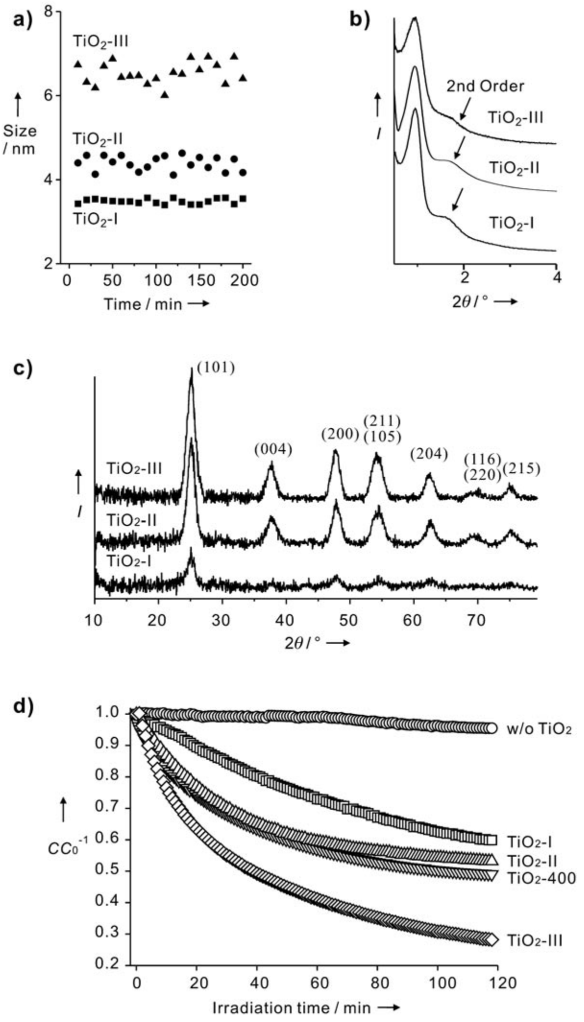

Figure 4. Effect of adding controlled quantities of water in the precursor solution on the crystallinity. a) Evolution of the sizes of the precursor particles monitored by DLS. b) SAXRD patterns. c) WAXRD patterns. d) Photodegradation of methylene blue (MB) over time by different TiO_2 samples.

The crystallinity and surface areas of semiconducting particles (e.g., TiO_2) are two very important factors in determining their photocatalytic performance.[24] The preliminary data of our highly crystalline and high-surface-area submicrometer-sized mesoporous TiO_2 spheres show great potential for photocatalytic applications. The photocatalytic activities of TiO_2-I, TiO_2-II, TiO_2-III, and TiO_2-400 were determined by the photocatalyzed degradation of methylene blue (MB) carried out under irradiation by UV light (365 nm). After calculated amounts of the TiO_2 samples were dispersed in the MB solutions, the UV/Vis absorbance spectra of the reaction solutions were recorded in situ as a function of the irradiation time to determine the concentration of MB remaining in the solutions. Figure 4d shows the decrease in MB concentration versus time under UV light irradiation. The increase in the photocatalytic activity with increasing anatase crystallinity is clearly shown. After 100 min of irradiation, 35 %, 45 %, 68 %, and 49 % of MB were degraded for TiO_2-I, TiO_2-II, TiO_2-III, and TiO_2-400 respectively. TiO_2-I has the lowest photocatalytic activity, which is due to it having the lowest crystallinity of the framework. The activity is maximal for TiO_2-III owing to the coexistence of high crystallization and a high surface area.

TiO_2-400 exhibits a lower activity than TiO_2-III in spite of their similar crystallinity, owing to its smaller surface area (Table 1).

In summary, we have developed a facile and highly efficient synthetic strategy for producing various ordered single- and multicomponent mesoporous metal oxide spheres at a rate of several grams per hour. The integration of the AASA process and AcHE sol-gel chemistry allows for the creation of high-surface-area mesoporous spheres with high framework crystallinity in a wide range of chemical compositions that are not readily accessible by other methods. The photocatalytic activity study serves as an example to demonstrate the structure–function relationship in which high surface areas and high crystallinity can significantly improve catalytic performance.

Experimental Section

The setup for the aerosol-assisted self-assembly process is illustrated in the Supporting Information (Figure S1). A home-made aerosol generator was employed; N_2 was used as the carrier gas. In a typical synthesis of mesostructured spheres, metal oxide precursors, acetic acid, HCl (37 wt%), and a calculated amount of water (for TiO_2-I, TiO_2-II, and TiO_2-III) were dissolved in ethanol. To form nanometer-sized stable metal oxo–acetate precursor particles without disruption by amphiphilic block copolymers, amphiphilic copolymer F127 ($EO_{106}PO_{70}EO_{106}$, $M_w = 12000\,g\,mol^{-1}$) was added to the solutions after stirring for 2 h. The solutions were stirred vigorously for one more hour before the aerosol spray process. During the aerosol spray process, the aerosol droplets were allowed to dry and start the surfactant-directed assembly in the 100 °C assembly chamber before passing through the heating zone set at 400 °C. When excess water was added in the precursor solutions, the temperature of the assembly chamber was raised to 120 °C. The resultant powder product was collected on 220 nm filter paper. The reactor was operated at a volumetric flow rate of 5 L (STP) min^{-1}. The residence time of the aerosol droplets is estimated to be about 5 s for both the assembly and heating chamber at such a flow rate. Faster flow rates increase the production efficiency, but less-ordered structures or even hollow spheres were generated (see the Supporting Information, Figure S3a,b). These as-synthesized mesostructured hybrid spheres were then calcined at desired temperatures (ramp rate 1 °C min^{-1}) in air for several hours to obtain mesoporous spheres. The molar ratios of the components in the precursor solutions of different systems were optimized as follows (water from concentrated HCl is not listed): 1) 1 $Ti(OBu)_4$: 4 acetic acid : 1.2 HCl:20 EtOH : 0.01 F127; 2) 1 $Al(OBu)_3$: 4 acetic acid : 2.4 HCl : 20 EtOH : 0.01 F127; 3) 1 $Zr(OBu)_4$: 4 acetic acid : 2.4 HCl : 20 EtOH : 0.01 F127; 4) 1 $Ti(OBu)_4$: 4 acetic acid : 1.2 HCl : 20 EtOH : 0.02 F127 : 0.1 $Cu(NO_3)_2$: 20 H_2O (excess); 5) 1 $Al(OBu)_3$: 1 $Si(OC_2H_5)_4$: 4 acetic acid : 1.2 HCl : 20 EtOH : 0.01 F127; 6) 1 $BaTi[OCH_2CH(CH_3)OCH_3]_6$: 8 acetic acid : 20 EtOH : 0.03 F127.

XRD patterns were obtained on a Scintag PADX diffractometer using $Cu_{K\alpha}$ radiation. SEM studies were performed on a FEI XL30 microscope operating at 2–5 keV. TEM studies were carried out on a FEI-T20 microscope operating at 200 keV. Nitrogen adsorption and desorption isotherms were measured using a Micromeritics TriStar 3000 system at liquid nitrogen temperature. Real-time UV/Vis extinction spectra were monitored with a fiber-optic spectrometer. The wavelength of the UV light source used for photocatalytic characterization is 365 nm (250 W).

Received: May 28, 2008

Keywords: mesoporous materials · metal oxides · photocatalysis · submicrospheres · titanates

[1] A. Taguchi, F. Schüch, *Microporous Mesoporous Mater.* **2005**, *77*, 1–45.

[2] C. Z. Yu, B. Z. Tian, D. Y. Zhao, *Curr. Opin. Solid State Mater. Sci.* **2003**, *7*, 191–197.

[3] Y. F. Lu, H. Y. Fan, A. Stump, T. L. Ward, T. Rieker, C. J. Brinker, *Nature* **1999**, *398*, 223–226.

[4] C. J. Brinker, Y. F. Lu, A. Sellinger, H. Y. Fan, *Adv. Mater.* **1999**, *11*, 579–585.

[5] Y. F. Lu, H. Y. Fan, N. Doke, D. A. Loy, R. A. Assink, D. A. LaVan, C. J. Brinker, *J. Am. Chem. Soc.* **2000**, *122*, 5258–5261.

[6] G. V. R. Rao, G. P. López, J. Bravo, H. Pham, A. K. Datye, H. F. Xu, T. L. Ward, *Adv. Mater.* **2002**, *14*, 1301–1304.

[7] N. Baccile, D. Grosso, C. Sanchez, *J. Mater. Chem.* **2003**, *13*, 3011–3016.

[8] B. Alonso, A. Douy, E. Véron, J. Perez, M.-N. Rager, D. Massiot, *J. Mater. Chem.* **2004**, *14*, 2006–2016.

[9] S. Areva, C. Boissière, D. Grosso, T. Asakawa, C. Sanchez, M. Lindén, *Chem. Commun.* **2004**, 1630–1631.

[10] X. L. Ji, Q. Y. Hu, J. E. Hampsey, X. P. Qiu, L. X. Gao, J. B. He, Y. F. Lu, *Chem. Mater.* **2006**, *18*, 2265–2274.

[11] X. M. Jiang, C. J. Brinker, *J. Am. Chem. Soc.* **2006**, *128*, 4512–4513.

[12] T. A. Ostomel, Q. H. Shi, C.-K. Tsung, H. J. Liang, G. D. Stucky, *Small* **2006**, *2*, 1261–1265.

[13] D. Grosso, G. J. de A. A. Soler Illia, E. L. Crepaldi, B. Charleux, C. Sanchez, *Adv. Funct. Mater.* **2003**, *13*, 37–42.

[14] C. Boissière, L. Nicole, C. Gervais, F. Babonneau, M. Antonietti, H. Amenitsch, C. Sanchez, D. Grosso, *Chem. Mater.* **2006**, *18*, 5238–5243.

[15] Y. Yan, F. Q. Zhang, Y. Meng, B. Tu, D. Y. Zhao, *Chem. Commun.* **2007**, 2867–2869.

[16] L. Li, C.-K. Tsung, Z. Yang, G. D. Stucky, L. D. Sun, J. F. Wang, C. H. Yan, *Adv. Mater.* **2008**, *20*, 903–908.

[17] J. Fan, S. W. Boettcher, G. D. Stucky, *Chem. Mater.* **2006**, *18*, 6391–6396.

[18] S. W. Boettcher, J. Fan, C.-K. Tsung, Q. H. Shi, G. D. Stucky, *Acc. Chem. Res.* **2007**, *40*, 784–792.

[19] J. Joo, T. Yu, Y. W. Kim, H. M. Pak, F. X. Wu, J. Z. Zhang, T. Hyeon, *J. Am. Chem. Soc.* **2003**, *125*, 6553–6557.

[20] M. Kuemmel, D. Grosso, C. Boissière, B. Smarsly, T. Brezesinski, P. A. Albouy, H. Amenitsch, C. Sanchez, *Angew. Chem.* **2005**, *117*, 4665–4668; *Angew. Chem. Int. Ed.* **2005**, *44*, 4589–4592.

[21] X. Y. Lai, X. T. Li, W. C. Geng, J. C. Tu, J. X. Li, S. L. Qiu, *Angew. Chem.* **2007**, *119*, 752–755; *Angew. Chem. Int. Ed.* **2007**, *46*, 738–741.

[22] Z. Y. Wu, Y. M. Wang, W. W. Huang, J. Yang, H. J. Wang, J. H. Xu, Y. L. Wei, J. H. Zhu, *Chem. Mater.* **2007**, *19*, 1613–1625.

[23] G. J. A. A. Soler-Illia, E. L. Crepaldi, D. Grosso, C. Sanchez, *J. Mater. Chem.* **2004**, *14*, 1879–1886.

[24] J. Tang, Y. Y. Wu, E. W. McFarland, G. D. Stucky, *Chem. Commun.* **2004**, 1670–1671.